# Enhanced Blocking Frequencies in Very-high Resolution Idealized Climate Model Simulations

**P. De Luca[1,2], B. Jiménez-Esteve[3], L. Degenhardt[2], S. Schemm[4], and S. Pfahl[2]**

[1]Barcelona Supercomputing Center (BSC), Barcelona, Spain.

[2]Institute of Meteorology - Freie Universität Berlin, Berlin, Germany

[3]Instituto de Geociencias (IGEO), Consejo Superior de Investigaciones Científicas–Universidad Complutense de Madrid (CSIC–UCM), Madrid, Spain

[4]Institute for Atmospheric and Climate Science - ETH Zürich, Zürich, Switzerland

Corresponding author: Paolo De Luca ([paolo.deluca@bsc.es](mailto:paolo.deluca@bsc.es))

**Key Points:**

- Blocking frequency increases downstream and poleward of sea-surface temperature front with convection permitting atmospheric resolution
- The specific region of increased blocking depends on the blocking index
- Changes in diabatic heating and Rossby wave breaking play a fundamental role for the blocking enhancement

**Keywords**: very-high resolution; climate modeling; ICON; idealized; blocking; wave breaking

**Abstract**

22

23  Atmospheric blocking is a key dynamical phenomenon in the mid- and high latitudes, able to drive
24  day-to-day weather changes and meteorological extremes such as heatwaves, droughts and cold
25  waves. Current global circulation models struggle to fully capture observed blocking frequencies,
26  likely because of their coarse horizontal resolution. Here we use convection permitting, nested
27  idealized model simulations for quantifying changes in blocking frequency and Rossby wave
28  breaking compared to a coarser resolution reference. We find an increase in blocking frequency
29  poleward and downstream of the area with increased resolution, while the exact regions depend
30  on the blocking index. These changes are probably due to a more accurate representation of
31  small-scale processes such as diabatic heating, which affect Rossby wave breaking and blocking
32  formation downstream. Our results thus suggest an improved representation of blocking in the
33  next generation of high-resolution global climate models.

34

35  **Plain Language Summary**

36  Atmospheric blocking is a persistent weather pattern associated with high-pressure anomalies
37  that is able to drive meteorological extremes such as heatwaves and drought in summer, and
38  cold waves in winter. Having blocking well represented in state-of-the-art climate models is of
39  paramount importance, however these models fail in simulating the frequency of blocking
40  events, likely because their grid resolution is not high enough for resolving small scale physical
41  processes important for the development of blocking episodes. Here we use very-high resolution
42  model simulations for quantifying blocking frequencies and the mechanisms driving these
43  episodes. Our simulations are idealised, in the sense that they do not fully represent the Earth's
44  system but allow us to focus on key physical mechanisms driving the blocking events. Our results
45  show that using a very-high resolution enhances blocking frequencies when compared to a lower
46  resolution grid. The findings point toward the importance that unresolved physical processes play
47  in generating blocking events that can only be simulated at very-high resolution and can be of
48  importance for the next generation of climate models.
49

50

## 1. Introduction

51

52  Atmospheric blocking can be considered one of the major features of the mid-latitude circulation

53  that occurs during an anomalous and persistent meandering of the jet stream (Lupo, 2021;

54  Nakamura & Huang, 2018; Woollings et al., 2018). Blocking is defined as a persistent weather

55  pattern, characterized by anticyclonic circulation, high surface pressure and blocked westerlies.

56  Changes in surface temperature, precipitation and wind patterns associated with blocking in turn

57  can evolve into severe weather extremes such as heatwaves and droughts in summer as well as

58  cold waves and low air quality during winter (e.g. Cai et al., 2020; Kautz et al., 2022; Matsueda,

59    2011; Pfahl & Wernli, 2012). Thus, it is of paramount importance to accurately represent blocking

60    in state-of-the-art coupled climate models to be able to anticipate future changes in the

61    associated extremes events under anthropogenic climate change.

62

63    Atmospheric blocking is currently underrepresented in coupled climate models (Davini &

64    D'Andrea, 2020; Pithan et al., 2016; Schiemann et al., 2020; Woollings et al., 2018). Such large

65    biases in the representation of blocking eventually lead to large uncertainties in its future climate

66    projections and, therefore, in representing dynamic mechanisms driving extreme weather

67    phenomena (e.g. heatwaves and droughts). The causes of the underestimation of blocking in

68    climate models are manifold. For example, Pithan et al. (2016) show that a better representation

69    of orographic drag can improve the simulation of European blocking. On the other hand, Scaife

70    et al. (2010) argue that blocking underestimation in climate models relates to the models'

71    climatological mean state bias. They suggest that correcting these mean-state biases improves

72    the representation of blocking and this is in agreement with Narinesingh et al. (2020), who

73    demonstrate, using aquaplanet simulations with idealized orographic forcing, that the mean

74    state highly impacts the blocking frequency climatology.

75

76    Another reason for the underestimation of blocking in the latest generation of global climate

77    models, or the Coupled Model Intercomparison Project Phase 6 (CMIP6) models (Eyring et al.,

78    2016), is the horizontal model resolution (Schiemann et al., 2020). Studies show that, to simulate

79    atmospheric blocking, a high horizontal resolution is necessary to capture smaller-scale processes

80    such as eddy vorticity fluxes (e.g. Yamazaki & Itoh, 2013) and diabatic heating in clouds (Pfahl et

81    al., 2015), which in turn sustain blocking events. Schiemann et al. (2020) compare blocking

82    frequency and persistence between CMIP6 and CMIP5 (Taylor et al., 2012) models, and also use

83    HighResMIP simulations (Haarsma et al., 2016) to quantify the effect of horizontal resolution.

84    They find that CMIP6 models better simulate blocking frequency and persistence compared to

85    CMIP5 and that an increase in horizontal resolution in HighResMIP simulations enhances blocking

86    frequency but not persistence in the northern mid-latitudes (Schiemann et al., 2020). Matsueda

87    et al. (2009) investigated future changes in blocking using different horizontal grid spacing, from

88    20 km to 180 km, in atmospheric global circulation models, and they state that the highest

89    horizontal resolution (i.e. 20 km) is required for properly simulating Euro-Atlantic blocking

90    events. In their follow-up study (Matsueda et al., 2010), where they assess future changes in

91    summer and wintertime blocking over Australia-New Zealand and in the Andes, they also show

92    similar conclusions. In addition, Athanasiadis et al. (2022) demonstrate how climate models' sea-

93    surface temperature cold biases in the central North Atlantic can be improved by deploying an

94    increased horizontal resolution in the ocean. They also show that such bias improvement leads

95    to changes in baroclinicity and diabatic heating, eventually enhancing European blocking events.

96    Scaife et al. (2011) also show that an improvement of the cold North Atlantic oceanic bias,

97    obtained with a higher resolution, leads to improved Atlantic winter blocking frequencies.

98    Despite this importance of horizontal resolution, so far and to our knowledge, there is a lack of a

99    study investigating the representation of blocking and its underlying mechanisms in climate

100   model simulations with km-scale horizontal resolution that allows for an explicit representation

101   of convective processes.

102

103   Diabatic heating in ascending air masses plays an important role for blocking formation and

104   maintenance downstream (Hermoso et al., 2024; Pfahl et al., 2015; Steinfeld et al., 2020;

105   Steinfeld & Pfahl, 2019). The ascending air is typically associated with the warm conveyor belt

106   (WCB) of extratropical cyclones, which subsequently forms a negative potential vorticity (PV)

107   anomaly in its outflow region, reinforcing anticyclonic circulation anomalies at upper levels in a

108   developing ridge. Preferred regions for such WCBs are the SST fronts over the western North

109   Atlantic and North Pacific, where many extratropical cyclones develop (Madonna et al., 2014).

110   The formation of a blocking event is thus intrinsically linked to the baroclinic instability and

111   cyclogenesis of extratropical cyclones along the SST-front over the western boundary currents

112   (Steinfeld & Pfahl, 2019; Yamamoto et al., 2021). Here, we hypothesize that an increase in

113   horizontal resolution in this area of SST-front increases diabatic processes linked to cyclone

114   formation and thus increases the WCB outflow that enhances ridge building, anticyclonic flow

115   and eventually blocking formation.

116

117 To explore this hypothesis, we build on previous work addressing the impact of horizontal

118 resolution on the simulation of blocking frequencies (e.g. Matsueda et al., 2009; Schiemann et

119 al., 2020) and on improvements of storm-track biases in climate models (Schemm, 2023). We

120 specifically make use of idealized aquaplanet climate model simulations with km-scale resolution

121 and convection permitting limited to a region with an artificial SST front where, climatologically,

122 diabatic heating associated with cyclogenesis occurs most frequently (Schemm, 2023). The SST-

123 front mimics the zonal asymmetries imposed by the land-sea contrast and the Gulf Stream SST.

124 Working with an aquaplanet enables us to better isolate the role that horizontal resolution has

125 in favoring blocking events in the absence of other confounding factors (e.g. orography). We,

126 therefore, investigate how such an idealized simulation can impact wintertime blocking

127 frequencies downstream of a zonal asymmetry. We also address the generative mechanisms of

128 the blocking events by conducting a Rossby-wave breaking analysis.

129

130 Section 2 describes the data and methods and, Section 3 shows our results in terms of blocking

131 averages, difference maps of blocking frequencies, and wave-breaking analysis. Lastly, Section 4

132 contains the discussion and conclusions of our study.

133

134 **2.  Data and Methods**

135 **2.1 Model simulations**

136 We use the idealized climate model simulations from Schemm (2023). These simulations were

137 conducted with the ICOsahedral Non-hydrostatic weather and climate model (ICON) v2.6.4 (Zängl

138 et al., 2015) in an aquaplanet setup. It includes parameterizations that follow the German

139 Weather Service (DWD) operational standard configuration, such as a one-moment two-category

140 microphysics scheme (Doms et al., 2011), non-orographic gravity wave drag (Orr et al., 2010), a

141 prognostic TKE scheme for sub-gridscale turbulent transfer (Raschendorfer, 2001), and the

142 radiation scheme ecRad (Hogan & Bozzo, 2018). The model has a global horizontal resolution of

143 ~20 km (R2B7), a time step of 180 s and parameterized deep convection following Tiedtke (1989).

144 A first regional nest with 10 km (R2B8) resolution employs a reduced scheme for shallow

145 convection and in a second nest with, 5 km (R2B9) resolution, convection is not parameterized.

146   The two inner nests also interact bi-directionally and work with a smaller time step that is

147   reduced by a factor of two, i.e., to 90 s and 45 s, respectively. They are located in the northern

148   hemisphere (NH), and centered around the SST front, as illustrated in Figure S1. Both NH and

149   southern hemisphere (SH) follow observed NH wintertime (DJF) zonal mean conditions and in

150   both hemispheres an idealized SST anomaly is superimposed on the zonally symmetric

151   background SST (termed "Qbos", see Neale & Hoskins (2000)), so that it can mimic the Gulf

152   Stream and the land-sea contrasts over the coast of North America (Schemm, 2023). The

153   simulations initially run for 10 perpetual years, with the solar zenith angle fixed over the equator

154   at 90° as is common practice in aquaplanet studies. Besides the high-resolution nest, both

155   hemispheres are symmetric. In order to quantify the influence of the km-scale resolution nest

156   globally, the simulations are regridded to a common horizontal grid of 1°x1° and daily mean data

157   are analyzed. Out of the original 10 perpetual winter years of simulations from Schemm (2023),

158   we use a total of 1,315 days (i.e. 3.65 perpetual winter years or 14.6 winter seasons) which were

159   the only ones available at the time of starting this study. For all our analyses, we use geopotential

160   height at 500 hPa (Z500, m) and zonal U wind at 300 hPa (m s$^{-1}$). More details on the ICON

161   simulations can be found in Schemm (2023).

162

163       **2.2 Blocking and Rossby-wave breaking indices**

164   We compute blocking by using geopotential at the 500 hPa level (Z500) and two algorithms

165   denoted as the Anomaly (ANM, similar to Schwierz et al., 2004) and Absolute (ABS, similar to

166   Davini et al., 2012) methods following Woollings et al. (2018). Both indices identify blocking

167   occurrences, but they are based on different characteristics of the atmospheric flow, hence their

168   results are not necessarily supposed to coincide (Scherrer et al., 2006; Woollings et al., 2018).

169

170   For computing blocking frequencies with the ANM method, we use the Contrack python package

171   (Steinfeld et al., 2020). We compute daily Z500 anomalies at grid-point level as the daily mean

172   departure from the daily mean climatology within the study period (no seasonality is present).

173   Then, daily blocking events are computed as 2-D regions with Z500 anomalies larger than the 90$^{th}$

174   percentiles of the daily Z500 anomaly distribution of all grid points between 50°-80°N, which

175    corresponds to 174 geopotential meters (gpm). We apply the same anomaly threshold to all grid

176    points to detect instantaneous blocking. To guarantee quasi-stationarity and persistence we also

177    impose a 50% minimum spatial overlap between the areas where instantaneous blocking occurs

178    for each consecutive time step over a total period (lifetime) of at least 5 days. Note that the

179    temporal granularity of our data is daily, compared to 6-hourly in many other studies, and hence

180    we use a smaller overlap. We have tested the sensitivity to different values of overlap and

181    anomaly threshold (see Supplementary Information) and found that the results are not very

182    sensitive to the exact threshold chosen. However, the blocking frequency quickly decreases if a

183    too-large overlap is chosen.

184

185    In the ABS method, areas are identified where the Z500 meridional gradient reverses. For

186    computing blocking frequencies with the ABS method, we use the R package MiLES which is

187    based on Davini et al. (2012) and additionally described in Davini (2018) and Woollings et al.

188    (2018). The ABS method interpolates the data to 2.5°x2.5° horizontal resolution and checks, at

189    each longitude, if Z500 decreases by at least 10m/° over a 15° segment north of the grid cell and,

190    in addition, also decreases over a 15° segment to the south (see Eqs. A1-A3 in Davini et al. (2012)).

191    Then, a grid point is defined as large-scale blocking if this condition is satisfied for at least a 15°

192    continuous longitude and a blocking event occurs, if a large-scale blocking is observed within a

193    5° latitude × 10° longitude box centered on that grid point with a persistence of at least 5 days.

194    In addition to this, Davini et al. (2012) also included additional criteria to determine if the reversal

195    of the Z500 field is associated with anticyclonic (AC-) or cyclonic (C-) Rossby wave breaking (RWB).

196    This distinction is made based on the zonal gradient of Z500 7.5° south of each blocked grid point,

197    with respectively Z500 decreasing (for AC-RWB) and increasing (for C-RWB) over a 7.5° East/West

198    segment centered at the blocking longitude. We note that the sum of AC-RWB and C-RWB events

199    is not equivalent to the ABS blocking events, because we consider large-scale, temporally

200    persistent blocking and not instantaneous blocking. For a complete derivation of the ABS and

201    Rossby-wave breaking indices we refer the reader to Appendix A and D in Davini et al. (2012).

202

203    We also check the statistical significance of both blocking and Rossby wave frequencies by

204    applying a two-sided z-test (Wilson, 1927) that compares two proportions, in our case being

205    percentage of the events at grid-point level, one from the NH and the corresponding one from

206    the SH. The z-test therefore tests the null hypothesis of whether the two proportions are

207    statistically equal and by obtaining a p-value <0.05 one rejects the null hypothesis and considers

208    the two proportions different with a 5% level of statistical significance.

209

## 3. Results

### 3.1 Blocking and Rossby-wave breaking average frequencies

212    Figure 1a-d shows the blocking frequencies (%), zonal wind averages (m s$^{-1}$) and the

213    corresponding zonal mean daily blocking frequencies for both the ANM and ABS methods. For

214    the ANM method, we observe a local maximum of ~11% of blocked days (out of 1315 days in

215    total) in both the SH and NH downstream/east of the SST-front (0-100°E) (Figure 1a). The zonal

216    average is above 6% blocking days around 65°N/S, i.e. poleward of the climatological position of

217    the 500hPa jet (Figure 1b). The ABS method, on the other hand, shows an overall maximum

218    frequency of ~7%, which is lower than for the ANM method, in both hemispheres (Figure 1c).

219    This difference is expected because the two blocking indices are intrinsically different, while the

220    ABS method identifies zones of geopotential reversal, the ANM method detects large and

221    persistent geopotential anomalies, which are not necessarily always related to reversals of the

222    mean flow. Moreover, we observe the peak number of blocking events at higher latitudes

223    compared to the ANM method, near the poleward limits of the study area (i.e. 75°N and 75°S,

224    Figure 1d). Lastly, there is a weak second maximum of ABS blocking over the subtropics (30°N

225    and 30°S, Figure 1d). Such reversals of the Z500 gradient in the subtropics are associated with

226    weaker Z500 anomalies (not captured by the ANM method) that typically are not even able to

227    'block' the zonal circulation in the midlatitudes. Zonal wind averages (m s$^{-1}$) show almost

228    symmetrical patterns between the NH and SH, with very weak values at the poles (i.e. 0-13 m s$^{-1}$

229    ) that gradually increase toward the lower midlatitudes (i.e. at 30°N-40°N and 30°S-40°S), where

230    they reach their maximum values of > 40 m s$^{-1}$ from 50°W to 50°E (Figure 1a), east of the SST

231    front (Schemm, 2023). As in observations, blocking and Rossby wave breaking, associated with a

232    reversal of the Z500 meridional gradient field as for the ABS blocking, tend to occur north of the

233    climatological jet stream location, (Davini et al., 2012), which underpins the fact that essential

234    blocking dynamics are captured by the idealized simulation. This pattern is also clearly shown in

235    Figure 1e-h, which represent the averages of both anticyclonic (AC-RWB) and cyclonic (C-RWB)

236    Rossby wave breaking events. When comparing our idealized blocking averages (Fig. 1a-d) with

237    previous studies using reanalysis products (Davini et al., 2012; Woollings et al., 2018) we notice

238    that our blocking frequencies are zonally more symmetric and the regional maxima are thus less

239    pronounced compared to reanalysis, which is due to the zonally more symmetric aquaplanet

240    setup that, e.g., does not feature land-sea contrasts. However, the meridional distributions of

241    our blocking frequencies resemble the ones of the reanalyses.

242
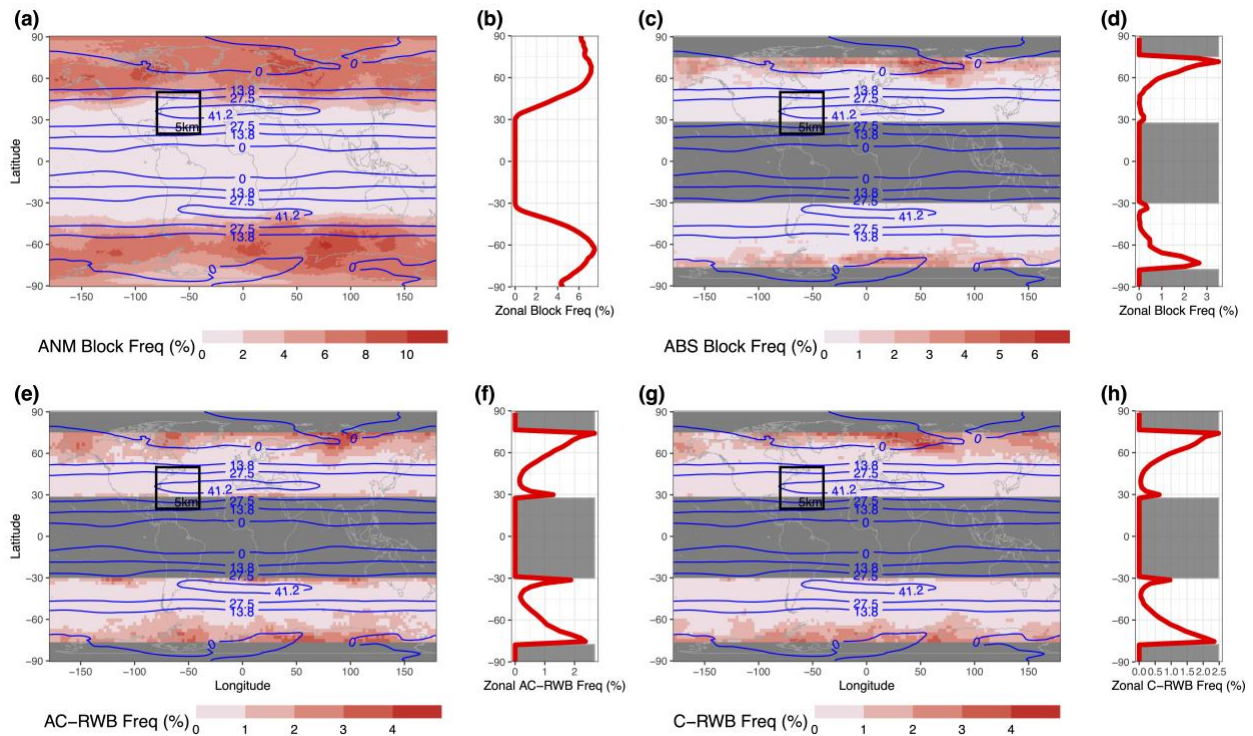


243

244    **Figure 1.** (a-d) Blocking and (e-h) Rossby-wave breaking average frequencies over the 14.6 boreal winter

245    seasons of the ICON simulation. Blocking frequencies in (a-b) and (c-d) are computed with the Anomaly

246    (ANM) and Absolute (ABS) method respectively. Rossby-wave breaking frequencies in (e-h) are computed

247    following Davini et al. (2012). Anticyclonic and cyclonic wave breaking are shown in (e-f) and (g-h)

248    respectively. In (b, d, f, h) the zonal frequencies of blocking and Rossby-wave breaking are presented. Blue

249    contour lines represent the zonal U wind averages at 500 hPa (m s$^{-1}$) over the same time-period. Black

250 boxes indicate the 5 km convection permitting area of the idealized simulation. Continents are only drawn
251 for illustrative purposes and are not present in the aquaplanet simulation.

252

253 **3.2 Changes in blocking and Rossby wave-breaking frequencies**

254 Figure 2 shows the blocking frequency difference between the NH, where the high-resolution,

255 convection permitting nests are located, and the SH, with a uniform resolution of 20 km. Results

256 for the ANM index point towards a significant (p-value <0.05) and widespread increase of

257 blocking frequency over the Arctic region, between northern Canada and Svalbard (note that

258 here land regions are only used as reference, as there is no representation of land in this

259 aquaplanet simulation). Such an increase in blocking frequency over this region is consistent with

260 what we would expect from a poleward shift and intensification of extratropical cyclones in the

261 SST front area as observed in Schemm (2023) and Hermoso et al. (2024), and an upper-

262 tropospheric outflow of low-PV air from the corresponding WCBs even further poleward .

263 Another region showing an increase in blocking frequencies is central western North America and

264 the northeastern Pacific, again associated with increased cyclone frequencies nearby to the

265 south/southwest. On the other hand, the blocking frequency decreases over northeastern North

266 America, eastern Europe and central Asia, which are regions where also the cyclone frequency

267 tends to decrease, associated with the general poleward shift of the storm tracks. Similar results

268 are obtained when changing the overlap area and the percentile threshold used in the blocking

269 identification algorithm, although with lower thresholds (i.e. $80^{th}$ and $85^{th}$ percentiles), the signal

270 over the Arctic gets weaker (Figure S2).

271

272 Differences for the ABS method show distinctive spatial patterns when compared to the ANM

273 method, with a significant increase in blocking frequency over Eurasia (50°E-100°E, 60°N) and

274 Alaska. The increase over Eurasia is located near the model's left-exit region of the jet streak

275 originating from the SST front (see again Fig. 1). It is also located to the east of the enhanced

276 northern hemispheric storm track's exit region, indicated by increased cyclone frequency

277 (Schemm, 2023). More intense extratropical cyclones due to increased resolution in the SST front

278 region may lead to enhanced wave breaking over that area at the end of their life cycle, which

279 leads to more frequent reversal of the geopotential height gradient as measured by the ABS

280  method. The difference between both method is hence an expected result because both

281  methods highlight different characteristics of blocking dynamics and Rossby wave breaking.

282

**(a)**



**(b)**



283
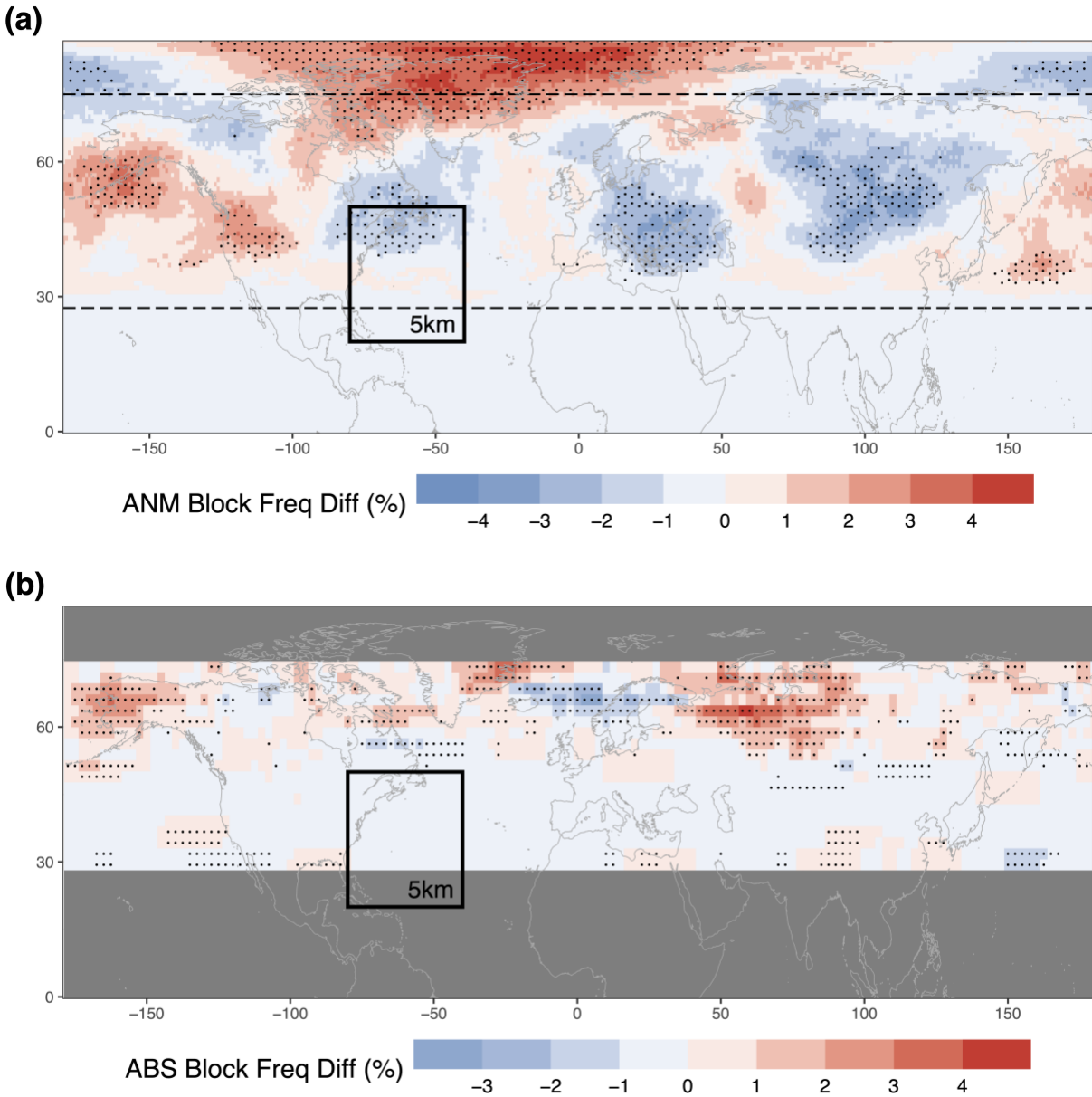
**Figure 2.** Difference between NH and SH for the (a) ANM and (b) ABS blocking frequencies (%). Stippling represents areas statistically significant at the 5% level (p-value <0.05) according to a proportion test. In (a) the two black horizontal dashed lines represent the geographical limits of (b) for comparison. Continents are only drawn for illustrative purposes and are not present in the aquaplanet simulation.

288

289   The enhanced ABS blocking frequency can be further decomposed into contributions from
290   anticyclonic and cyclonic wave breaking associated with a reversal of the Z500 meridional
291   gradient field (Davini et al., 2012), as shown in Fig. 3. While the increase over Alaska is almost
292   entirely due to an increase in anticyclonic wave breaking, the signal over Russia is related to both
293   enhanced cyclonic wave breaking in its western part and enhanced anticyclonic wave breaking
294   further east. This west-east dipole of cyclonic and anticyclonic wave breaking represents an
295   increase or extension of the wave breaking location, as the positive anomalies are larger than the
296   negative ones. This is expected from the strengthening and tilting of the storm track in the very-
297   high resolution hemisphere, as shown in Schemm (2023). The fact that wave breaking anomalies
298   occur in a west-east dipole provides evidence of the realistic representation of these dynamical
299   processes in our idealized model, since such a dipole is also present in the wave-breaking
300   climatology over the North Atlantic based on reanalysis data (Tamarin-Brodsky & Harnik, 2024).
301   We also computed Rossby-wave breaking difference maps following the methodology proposed
302   by Barnes & Hartmann (2012) and using Z500 instead of PV (Text S1 and Figure S3). This
303   alternative index shows consistent results, with a significant increase in anticyclonic and cyclonic
304   wave breaking in the same range of longitudes as the Davini et al. (2012) method.

305

**(a)**



**(b)**



306
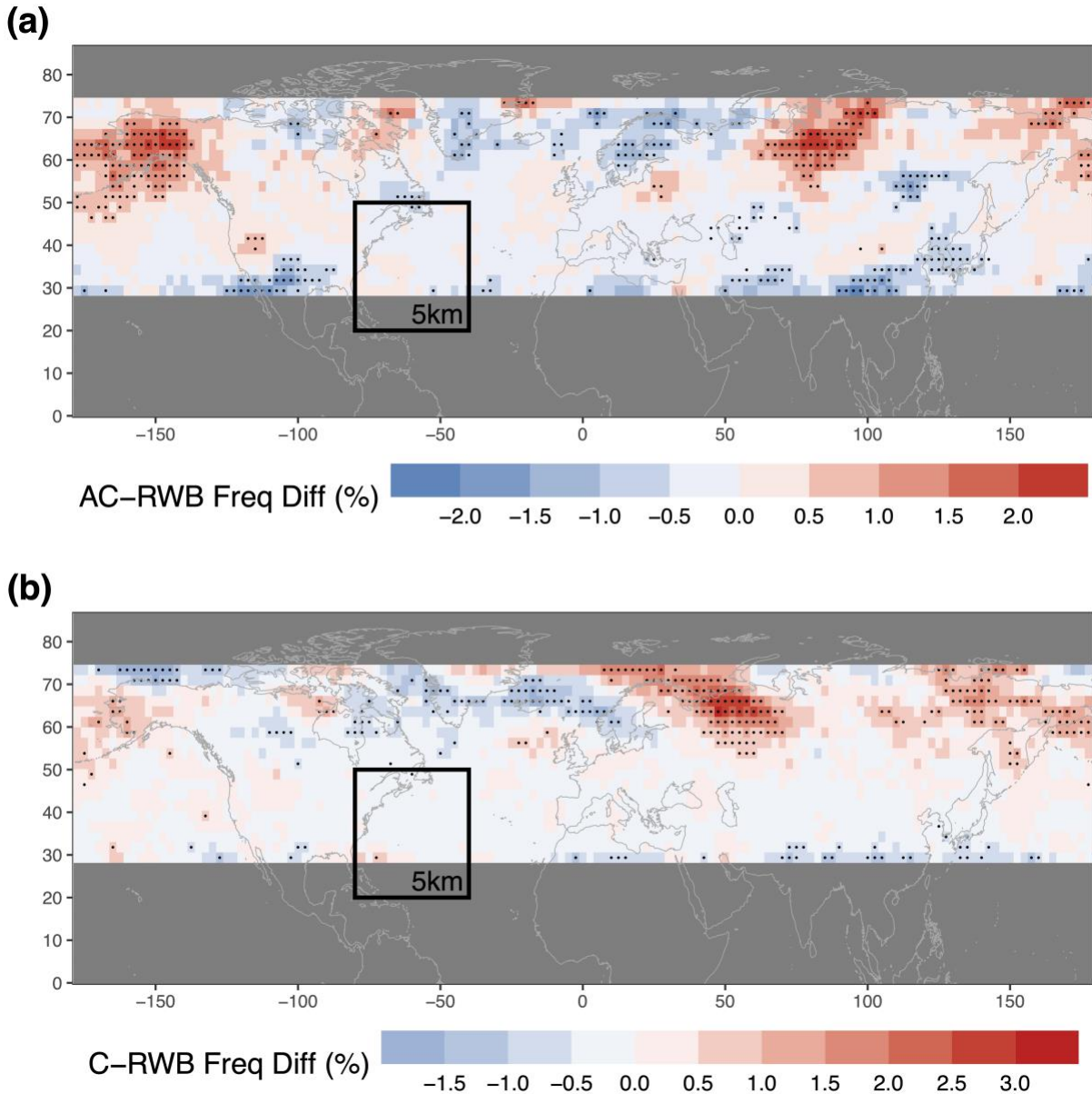
**Figure 3.** Difference maps of Rossby-wave breaking frequencies computed from a reversal of the Z500 meridional gradient field. (a) Anticyclonic and (b) cyclonic wave-breaking events computed following Davini et al. (2012). Stippling represent areas statistically significant at the 5% level (p-value <0.05) according to a proportion test. Continents are only drawn for illustrative purposes and are not present in the aquaplanet simulation.

312

### 4. Discussion and Conclusions

In this work, we have used an idealized very-high resolution convection permitting simulation with the ICON climate model in aquaplanet setup (Schemm, 2023) to quantify the impact of such

316     a high resolution on blocking and Rossby-wave breaking frequencies. We analyze a total of 14.6

317     boreal winter seasons, symmetrically in the SH (low) and NH (high resolution). To quantify the

318     impact of resolution on cyclone-related diabatic processes, the NH has been simulated with two

319     bi-directionally interacting nested grids of 10 and 5 km grid spacing centered around an idealized

320     SST front. The highest-resolution nested domain allows for convective processes to occur without

321     being parameterized. Our results indicate that increased resolution in the region of extratropical

322     cyclone growth leads to increased blocking frequencies. The exact region of enhanced blocking

323     occurrence depends on the blocking index. An index identifying stationary anticyclones indicates

324     more frequent blocking poleward of the region where also the cyclone frequency increases due

325     to a more explicit representation of diabatic processes with high resolution (Schemm, 2023). This

326     is consistent with the hypothesis that diabatic processes amplify cyclones and the associated

327     WCBs, leading to enhanced poleward outflow of low-PV air masses in the middle and upper

328     troposphere that reinforce stationary anticyclones (Pfahl et al., 2015; Steinfeld et al., 2020;

329     Steinfeld & Pfahl, 2019). On the contrary, an index associating blocking with a reversal of

330     meridional geopotential height contours and thus wave breaking rather indicates more frequent

331     blocking further downstream, east of the strengthened storm track, where the more frequent

332     cyclones are associated with enhanced cyclonic and anti-cyclonic wave breaking at the end of

333     their life cycle (Figure S4).

334

335     Previous studies (e.g. Athanasiadis et al., 2022; Matsueda et al., 2009; Scaife et al., 2011;

336     Schiemann et al., 2020) have already shown that increasing spatial resolution can be beneficial

337     for the representation of blocking in climate models. Due to the importance of diabatic

338     processes, going to even higher, convection permitting resolution is hypothesized to further

339     reduce blocking biases, but this has not been explicitly tested so far due to the lack of global

340     climate simulations with such high-resolution spanning sufficiently long periods. Here we have

341     corroborated this hypothesis based on an idealized aquaplanet setup. This may have important

342     implications also for the next generation of convection permitting global climate models. Current

343     climate models still underestimate blocking frequencies. In particular, they underestimate the

344     occurrence of stationary anticyclones (ANM blocking) over the North Atlantic and the occurrence

345  of wave breaking (ABS blocking) further downstream over Eurasia (Woollings et al., 2018). Our

346  results indicate that a higher resolution and better representation of diabatic processes over the

347  SST front may increase ANM blocking closer to this SST front region and ABS blocking further

348  downstream, thus potentially reducing both of these biases. This makes us optimistic that

349  blocking biases will be reduced in convection permitting global climate simulations, eventually

350  leading to more reliable estimates of changes of this important weather pattern in a warming

351  climate.

352

356

357  **Open Research**

358  The ICON simulation data, blocking and Rossby-wave breaking indices used in the study can be

359  obtained in the following open-source repository: https://doi.org/10.5281/zenodo.12575399.

360  Whereas the softwares used for computing the blocking and Rossby-wave breaking indices are

361  freely       available       in       the       next       GitHub       repositories:       i)

362  https://github.com/steidani/ConTrack/tree/master;  ii)  https://github.com/oloapinivad/MiLES

363  and iii) https://github.com/skaderli/WaveBreaking.

364

365  **References**

366  Athanasiadis, P. J., Ogawa, F., Omrani, N.-E., Keenlyside, N., Schiemann, R., Baker, A. J., et al.

367      (2022). Mitigating Climate Biases in the Midlatitude North Atlantic by Increasing Model

368      Resolution: SST Gradients and Their Relation to Blocking and the Jet. *Journal of Climate*,

369      *35*(21), 6985–7006. https://doi.org/https://doi.org/10.1175/JCLI-D-21-0515.1

370  Barnes, E. A., & Hartmann, D. L. (2012). Detection of Rossby wave breaking and its response to

371      shifts of the midlatitude jet with climate change. *Journal of Geophysical Research:*

372      *Atmospheres*, *117*(D9). https://doi.org/https://doi.org/10.1029/2012JD017469

373  Cai, W., Xu, X., Cheng, X., Wei, F., Qiu, X., & Zhu, W. (2020). Impact of "blocking" structure in

374       the troposphere on the wintertime persistent heavy air pollution in northern China.

375       *Science of The Total Environment*, *741*, 140325.

376       https://doi.org/https://doi.org/10.1016/j.scitotenv.2020.140325

377   Davini, P. (2018). MiLES - Mid Latitude Evaluation System. Zenodo.

378       https://doi.org/http://doi.org/10.5281/zenodo.1237837

379   Davini, P., & D'Andrea, F. (2020). From CMIP3 to CMIP6: Northern Hemisphere Atmospheric

380       Blocking Simulation in Present and Future Climate. *Journal of Climate*, *33*(23), 10021–

381       10038. https://doi.org/https://doi.org/10.1175/JCLI-D-19-0862.1

382   Davini, P., Cagnazzo, C., Gualdi, S., & Navarra, A. (2012). Bidimensional Diagnostics, Variability,

383       and Trends of Northern Hemisphere Blocking. *Journal of Climate*, *25*(19), 6496–6509.

384       https://doi.org/https://doi.org/10.1175/JCLI-D-12-00032.1

385   Doms, G., Förstner, J., Heise, E., Herzog, H.-J., Mironov, D., Raschendorfer, M., et al. (2011). *A*

386       *description of the nonhydrostatic regional COSMO model Part II: Physical parameterization*.

387   Eyring, V., Bony, S., Meehl, G. A., Senior, C. A., Stevens, B., Stouffer, R. J., & Taylor, K. E. (2016).

388       Overview of the Coupled Model Intercomparison Project Phase 6 (CMIP6) experimental

389       design and organization. *Geosci. Model Dev.*, *9*(5), 1937–1958.

390       https://doi.org/10.5194/gmd-9-1937-2016

391   Haarsma, R. J., Roberts, M. J., Vidale, P. L., Senior, C. A., Bellucci, A., Bao, Q., et al. (2016). High

392       Resolution Model Intercomparison Project (HighResMIP~v1.0) for CMIP6. *Geoscientific*

393       *Model Development*, *9*(11), 4185–4208. https://doi.org/10.5194/gmd-9-4185-2016

394   Hermoso, A., Rivière, G., Harvey, B., Methven, J., & Schemm, S. (2024). A dynamical

395       interpretation of the intensification of the winter North Atlantic jet stream in reanalysis.

396       *Journal of Climate*. https://doi.org/https://doi.org/10.1175/JCLI-D-23-0757.1

397   Hogan, R. J., & Bozzo, A. (2018). A Flexible and Efficient Radiation Scheme for the ECMWF

398       Model. *Journal of Advances in Modeling Earth Systems*, *10*(8), 1990–2008.

399       https://doi.org/https://doi.org/10.1029/2018MS001364

400   Kautz, L.-A., Martius, O., Pfahl, S., Pinto, J. G., Ramos, A. M., Sousa, P. M., & Woollings, T.

401       (2022). Atmospheric blocking and weather extremes over the Euro-Atlantic sector -- a

402       review. *Weather and Climate Dynamics*, *3*(1), 305–336. https://doi.org/10.5194/wcd-3-

403    305-2022

404    Lupo, A. R. (2021). Atmospheric blocking events: a review. *Annals of the New York Academy of*
405        *Sciences*, *1504*(1), 5–24. https://doi.org/https://doi.org/10.1111/nyas.14557

406    Madonna, E., Wernli, H., Joos, H., & Martius, O. (2014). Warm Conveyor Belts in the ERA-
407        Interim Dataset (1979–2010). Part I: Climatology and Potential Vorticity Evolution. *Journal*
408        *of Climate*, *27*(1), 3–26. https://doi.org/https://doi.org/10.1175/JCLI-D-12-00720.1

409    Matsueda, M. (2011). Predictability of Euro-Russian blocking in summer of 2010. *Geophysical*
410        *Research Letters*, *38*(6). https://doi.org/https://doi.org/10.1029/2010GL046557

411    Matsueda, M., Mizuta, R., & Kusunoki, S. (2009). Future change in wintertime atmospheric
412        blocking simulated using a 20-km-mesh atmospheric global circulation model. *Journal of*
413        *Geophysical Research: Atmospheres*, *114*(D12).
414        https://doi.org/https://doi.org/10.1029/2009JD011919

415    Matsueda, M., Endo, H., & Mizuta, R. (2010). Future change in Southern Hemisphere
416        summertime and wintertime atmospheric blockings simulated using a 20-km-mesh AGCM.
417        *Geophysical Research Letters*, *37*(2).
418        https://doi.org/https://doi.org/10.1029/2009GL041758

419    Nakamura, N., & Huang, C. S. Y. (2018). Atmospheric blocking as a traffic jam in the jet stream.
420        *Science*, *361*(6397), 42–47. https://doi.org/10.1126/science.aat0721

421    Narinesingh, V., Booth, J. F., Clark, S. K., & Ming, Y. (2020). Atmospheric blocking in an
422        aquaplanet and the impact of orography. *Weather and Climate Dynamics*, *1*(2), 293–311.
423        https://doi.org/10.5194/wcd-1-293-2020

424    Neale, R. B., & Hoskins, B. J. (2000). A standard test for AGCMs including their physical
425        parametrizations: I: the proposal. *Atmospheric Science Letters*, *1*(2), 101–107.
426        https://doi.org/https://doi.org/10.1006/asle.2000.0022

427    Orr, A., Bechtold, P., Scinocca, J., Ern, M., & Janiskova, M. (2010). Improved Middle Atmosphere
428        Climate and Forecasts in the ECMWF Model through a Nonorographic Gravity Wave Drag
429        Parameterization. *Journal of Climate*, *23*(22), 5905–5926.
430        https://doi.org/https://doi.org/10.1175/2010JCLI3490.1

431    Pfahl, S., & Wernli, H. (2012). Quantifying the relevance of atmospheric blocking for co-located

432      temperature extremes in the Northern Hemisphere on (sub-)daily time scales. *Geophysical*

433      *Research Letters*, *39*(12). https://doi.org/https://doi.org/10.1029/2012GL052261

434  Pfahl, S., Schwierz, C., Croci-Maspoli, M., Grams, C. M., & Wernli, H. (2015). Importance of

435      latent heat release in ascending air streams for atmospheric blocking. *Nature Geoscience*,

436      *8*(8), 610–614.

437  Pithan, F., Shepherd, T. G., Zappa, G., & Sandu, I. (2016). Climate model biases in jet streams,

438      blocking and storm tracks resulting from missing orographic drag. *Geophysical Research*

439      *Letters*, *43*(13), 7231–7240. https://doi.org/https://doi.org/10.1002/2016GL069551

440  Raschendorfer, M. (2001). *The new turbulence parameterization of LM*.

441  Scaife, A. A., Woollings, T., Knight, J., Martin, G., & Hinton, T. (2010). Atmospheric Blocking and

442      Mean Biases in Climate Models. *Journal of Climate*, *23*(23), 6143–6152.

443      https://doi.org/https://doi.org/10.1175/2010JCLI3728.1

444  Scaife, A. A., Copsey, D., Gordon, C., Harris, C., Hinton, T., Keeley, S., et al. (2011). Improved

445      Atlantic winter blocking in a climate model. *Geophysical Research Letters*, *38*(23).

446      https://doi.org/https://doi.org/10.1029/2011GL049573

447  Schemm, S. (2023). Toward Eliminating the Decades-Old "Too Zonal and Too Equatorward"

448      Storm-Track Bias in Climate Models. *Journal of Advances in Modeling Earth Systems*, *15*(2),

449      e2022MS003482. https://doi.org/https://doi.org/10.1029/2022MS003482

450  Scherrer, S. C., Croci-Maspoli, M., Schwierz, C., & Appenzeller, C. (2006). Two-dimensional

451      indices of atmospheric blocking and their statistical relationship with winter climate

452      patterns in the Euro-Atlantic region. *International Journal of Climatology*, *26*(2), 233–249.

453      https://doi.org/https://doi.org/10.1002/joc.1250

454  Schiemann, R., Athanasiadis, P., Barriopedro, D., Doblas-Reyes, F., Lohmann, K., Roberts, M. J.,

455      et al. (2020). Northern Hemisphere blocking simulation in current climate models:

456      evaluating progress from the Climate Model Intercomparison Project Phase~5 to 6 and

457      sensitivity to resolution. *Weather and Climate Dynamics*, *1*(1), 277–292.

458      https://doi.org/10.5194/wcd-1-277-2020

459  Schwierz, C., Croci-Maspoli, M., & Davies, H. C. (2004). Perspicacious indicators of atmospheric

460      blocking. *Geophysical Research Letters*, *31*(6).

461 https://doi.org/https://doi.org/10.1029/2003GL019341

462 Steinfeld, D., & Pfahl, S. (2019). The role of latent heating in atmospheric blocking dynamics: a

463 global climatology. *Climate Dynamics*, *53*(9), 6159–6180. https://doi.org/10.1007/s00382-

464 019-04919-6

465 Steinfeld, D., Boettcher, M., Forbes, R., & Pfahl, S. (2020). The sensitivity of atmospheric

466 blocking to upstream latent heating -- numerical experiments. *Weather and Climate*

467 *Dynamics*, *1*(2), 405–426. https://doi.org/10.5194/wcd-1-405-2020

468 Tamarin-Brodsky, T., & Harnik, N. (2024). The relation between Rossby wave-breaking events

469 and low-level weather systems. *Weather and Climate Dynamics*, *5*(1), 87–108.

470 https://doi.org/10.5194/wcd-5-87-2024

471 Taylor, K. E., Stouffer, R. J., & Meehl, G. A. (2012). An Overview of CMIP5 and the Experiment

472 Design. *Bulletin of the American Meteorological Society*, *93*(4), 485–498.

473 https://doi.org/https://doi.org/10.1175/BAMS-D-11-00094.1

474 Tiedtke, M. (1989). A Comprehensive Mass Flux Scheme for Cumulus Parameterization in Large-

475 Scale Models. *Monthly Weather Review*, *117*(8), 1779–1800.

476 https://doi.org/https://doi.org/10.1175/1520-0493(1989)117<1779:ACMFSF>2.0.CO;2

477 Wilson, E. B. (1927). Probable Inference, the Law of Succession, and Statistical Inference.

478 *Journal of the American Statistical Association*, *22*(158), 209–212.

479 https://doi.org/10.1080/01621459.1927.10502953

480 Woollings, T., Barriopedro, D., Methven, J., Son, S.-W., Martius, O., Harvey, B., et al. (2018).

481 Blocking and its Response to Climate Change. *Current Climate Change Reports*.

482 https://doi.org/10.1007/s40641-018-0108-z

483 Yamamoto, A., Nonaka, M., Martineau, P., Yamazaki, A., Kwon, Y.-O., Nakamura, H., & Taguchi,

484 B. (2021). Oceanic moisture sources contributing to wintertime Euro-Atlantic blocking.

485 *Weather and Climate Dynamics*, *2*(3), 819–840. https://doi.org/10.5194/wcd-2-819-2021

486 Yamazaki, A., & Itoh, H. (2013). Vortex–Vortex Interactions for the Maintenance of Blocking.

487 Part I: The Selective Absorption Mechanism and a Case Study. *Journal of the Atmospheric*

488 *Sciences*, *70*(3), 725–742. https://doi.org/https://doi.org/10.1175/JAS-D-11-0295.1

489 Zängl, G., Reinert, D., Rípodas, P., & Baldauf, M. (2015). The ICON (ICOsahedral Non-

490    hydrostatic) modelling framework of DWD and MPI-M: Description of the non-hydrostatic

491    dynamical core. *Quarterly Journal of the Royal Meteorological Society*, *141*(687), 563–579.

492    https://doi.org/https://doi.org/10.1002/qj.2378

493

494

495

496

497

498

499

500

501

502

503

504

505

506

507

508

509

510

511

512

513

514

515

516

517

518

519                    Supporting Information for

520   **Enhanced Blocking Frequencies in Very-high Resolution Idealized Climate Model**
521                            **Simulations**

522              P. De Luca[1,2], B. Jiménez-Esteve[3], L. Degenhardt[2], S. Schemm[4], and S. Pfahl[2]

523                   1. Barcelona Supercomputing Center (BSC), Barcelona, Spain

524               2. Institute of Meteorology - Freie Universität Berlin, Berlin, Germany

525   3. Instituto de Geociencias (IGEO), Consejo Superior de Investigaciones Científicas–Universidad Complutense de
526                        Madrid (CSIC–UCM), Madrid, Spain

527             4. Institute for Atmospheric and Climate Science - ETH Zürich, Zürich, Switzerland

528

529   **Contents of this file**
530

533

534   **Introduction**
535   This Supporting Information provides extra details on a second method used for computing Rossby-wave
536   breaking along with three supporting figures that describe the nested areas used in the idealized climate
537   model simulations, difference maps of ANM blocking frequencies computed with other overlapping areas
538   and percentiles than in the main text, and difference maps of Rossby-wave breaking computed with the
539   second method here described.

540
541

542   **Text S1.**
543   For computing anticyclonic and cyclonic wave-breaking frequencies we also use a second algorithm
544   introduced by Barnes & Hartmann (2012). This algorithm searches for synoptic-scale wave-breaking of a
545   given field by quantifying regions where the contours overturn using potential vorticity (PV) contours
546   (usually 2PVU is taken). In our case, as we do not have PV available, we have substituted PV for Z500 and
547   tested results using different contours but found that the 5300 gpm contour gives the most sensible result.
548   To quantify wave-breaking events, the longest closed contour encircling the field's pole is identified. Then,
549   the algorithm searches the locations where a single meridian intersects the contour at least three times. Such
550   locations are named overturning points, and if they occur within 500 km of each other and within the same
551   contour, they are considered part of the same event. Then, the algorithm groups the overturning contours
552   into daily wave-breaking events by quantifying contiguous contours that all have overturning centers (i.e.
553   geographic centers of the overturning points) within 2000 km of each other. If this condition is not fulfilled,
554   different wave-breaking events are created. The center of a wave-breaking event is defined as the
555   geographic center of all grid points on all contours in the event (Barnes & Hartmann, 2012).

556
557   The detection algorithm also differentiates between cyclonic and anticyclonic wave-breaking events, or
558   breaking events that overturn cyclonically and anticyclonically. In our case, when we use Z500 instead of

559  PV, this is done by ordering the overturning points from west to east, so that in the Northern hemisphere
560  cyclonic events are quantified as those whose west-most overturning point is equatorward of the east-most
561  overturning point and anticyclonic ones as those whose west-most overturning point is poleward of the
562  east-most overturning point. In the Southern Hemisphere the definition is the opposite. To consider the
563  possibility that one wave-breaking event lasts more than one day the algorithm also groups the events in
564  time that have a center within 2000 km of each other (Barnes & Hartmann, 2012). Here, we compute
565  cyclonic and anticyclonic Rossy wave-breaking by using daily Z500 fields at 1°x1° horizontal resolution
566  from the ICON simulation of Schemm (2023) and using the python library WaveBreaking v0.3.7 (Kaderli,
567  2023).

568
569
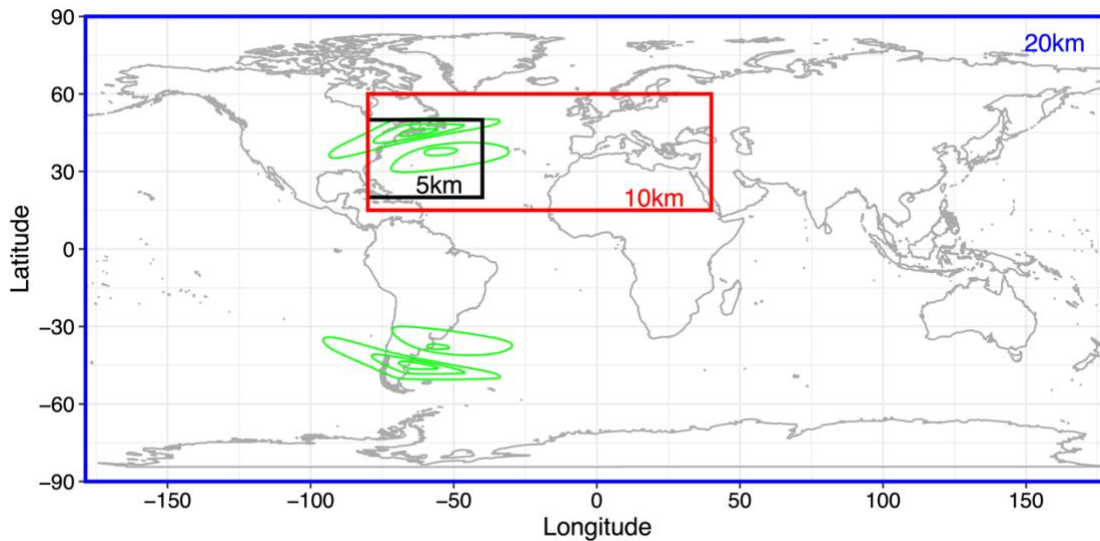


570
571  **Figure S1.** Horizontal resolution (km) of the nested areas used in the ICON simulations. Black: 5 km; red:
572  10 km; and blue: 20 km. These correspond to the same resolution and areas of Schemm (2023). Green
573  contours show the idealized sea-surface temperature front computed from 2m temperatures after removing
574  the zonal mean. Continents are only drawn for illustrative purposes and are not present in the aquaplanet
575  simulation.
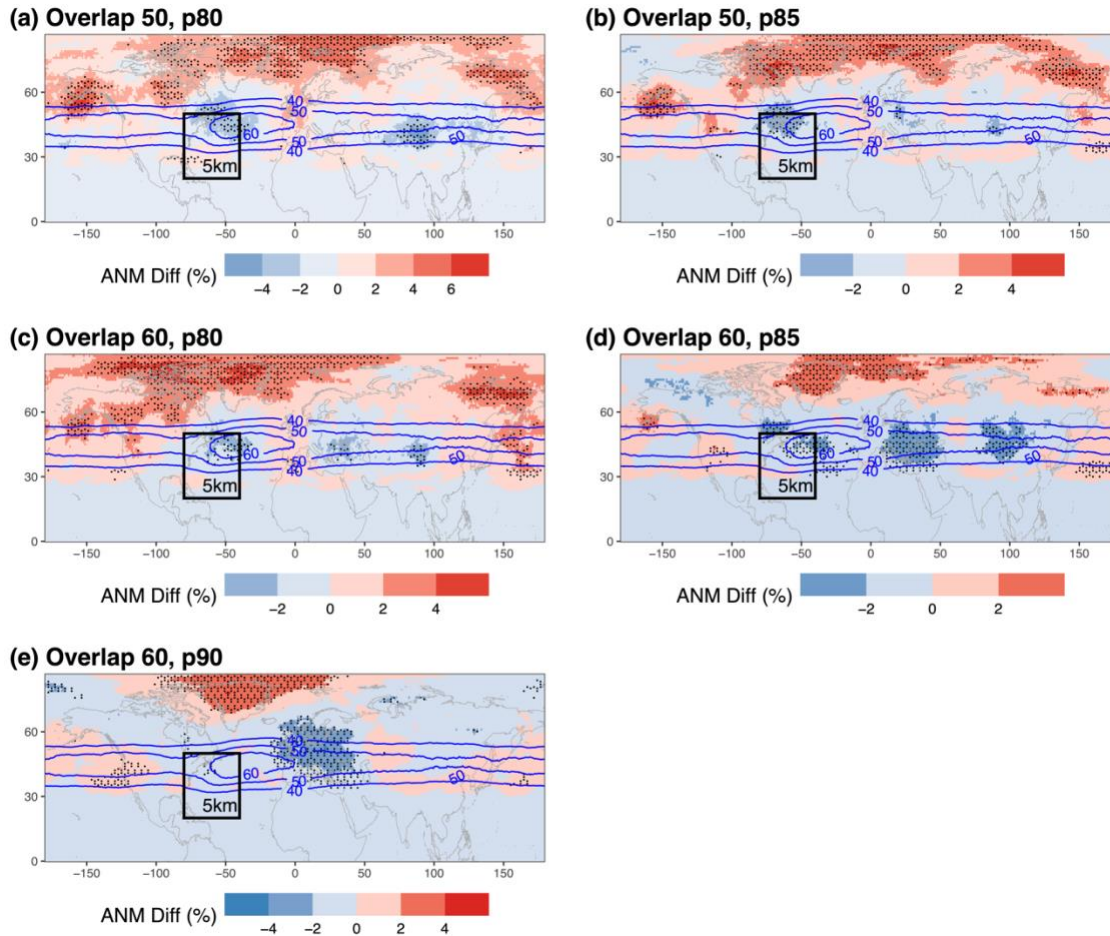
**Figure S2.** As Figure 2a but for ANM blocking frequency differences (%) computed with (a) overlap 50 and 80th percentile, (b) 50 and 85th, (c) 60 and 80th, (d) 60 and 85th and (e) 60 and 90th. Continents are only drawn for illustrative purposes and are not present in the aquaplanet simulation.
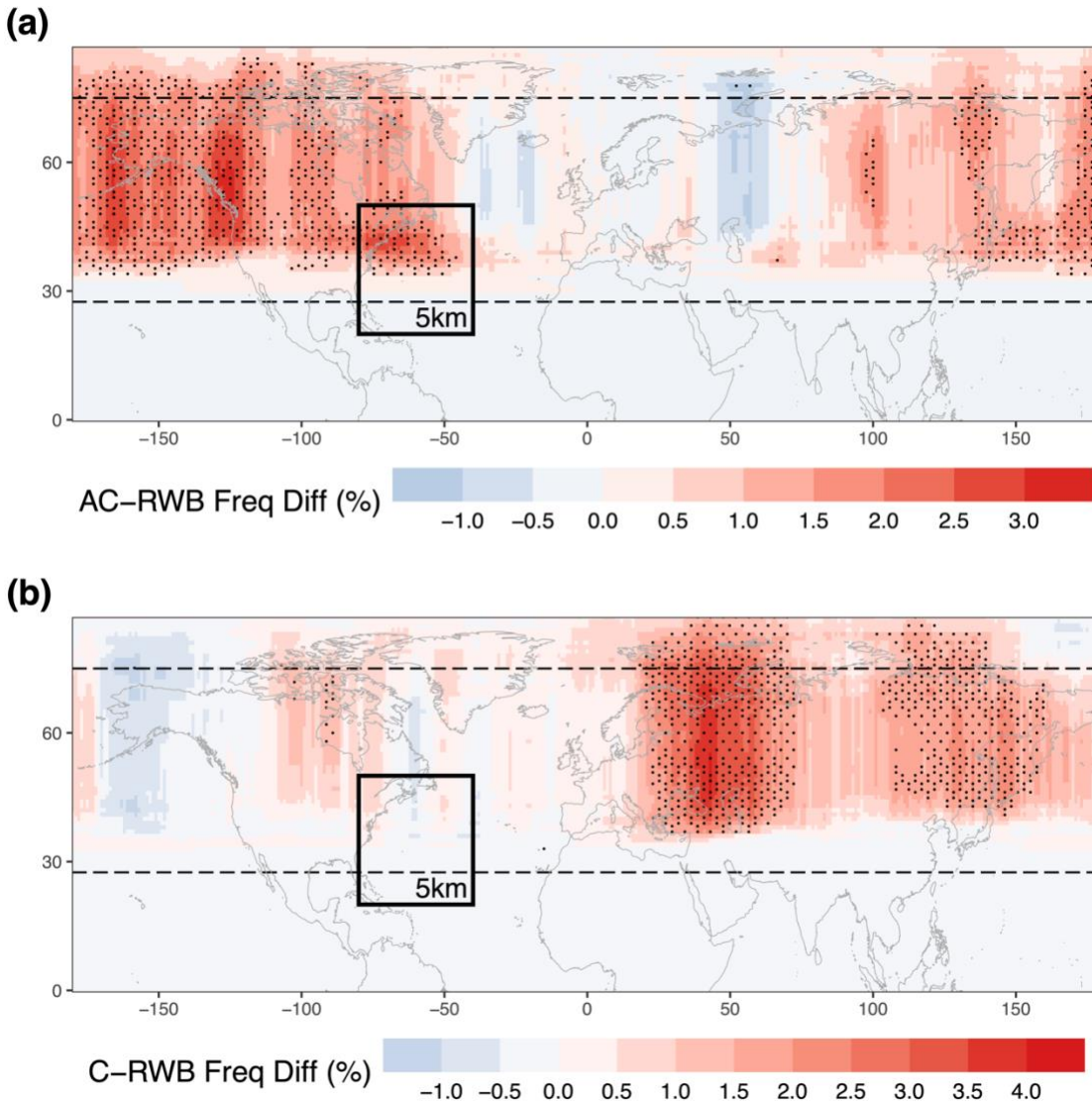
**Figure S3.** Same as Figure 3 but with Rossby-wave breaking computed following Barnes & Hartmann (2012). Black horizontal lines represent the geographical limits of the Davini et al. (2012) RWB method for comparison. Continents are only drawn for illustrative purposes and are not present in the aquaplanet simulation.
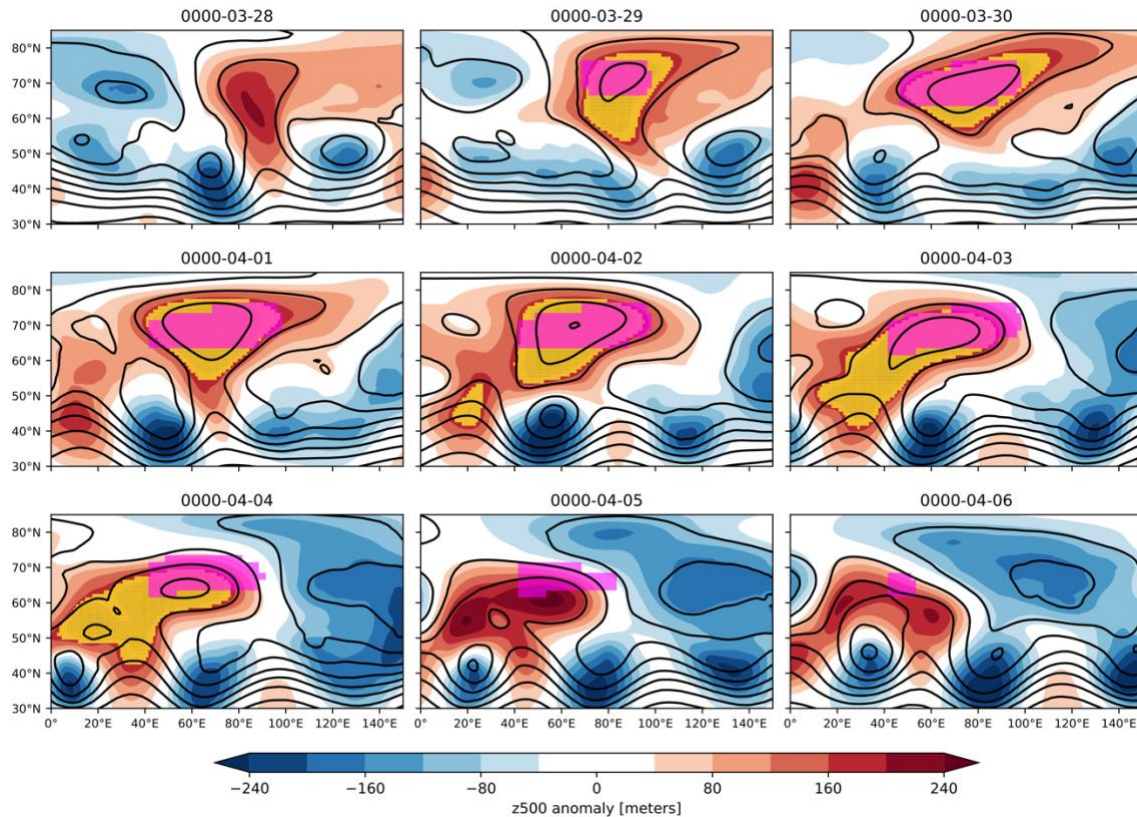
**Figure S4.** Case-study of a blocking event using geopotential height (m) anomalies at 500hPa (z500). Each panel represent a single day. Yellow and pink grid-points show respectively the ANM and ABS blocking indices.

**References**

Barnes, E. A., & Hartmann, D. L. (2012). Detection of Rossby wave breaking and its response to shifts of the midlatitude jet with climate change. *Journal of Geophysical Research: Atmospheres*, *117*(D9). https://doi.org/https://doi.org/10.1029/2012JD017469

Davini, P., Cagnazzo, C., Gualdi, S., & Navarra, A. (2012). Bidimensional Diagnostics, Variability, and Trends of Northern Hemisphere Blocking. *Journal of Climate*, *25*(19), 6496–6509. https://doi.org/https://doi.org/10.1175/JCLI-D-12-00032.1

Kaderli, S. (2023). WaveBreaking - Detection, Classification and Tracking of Rossby Wave Breaking. https://doi.org/https://doi.org/10.5281/zenodo.8123188

Schemm, S. (2023). Toward Eliminating the Decades-Old "Too Zonal and Too Equatorward" Storm-Track Bias in Climate Models. *Journal of Advances in Modeling Earth Systems*, *15*(2), e2022MS003482. https://doi.org/https://doi.org/10.1029/2022MS003482